Phase-field modeling of two-dimensional crystal growth with anisotropic diffusion

Esteban Meca,[1,*] Vivek B. Shenoy,[2,†] and John Lowengrub[3,‡]

[1]*Department of Mathematics, University of California, Irvine, California 92697-3875, USA*

[2]*Department of Materials Science and Engineering, University of Pennsylvania, Philadelphia, Pennsylvania 19104-6272, USA*

[3]*Departments of Mathematics and Chemical Engineering & Materials Science, University of California, Irvine, California 92697-3875, USA*

(Received 10 September 2013; published 27 November 2013)

In the present article, we introduce a phase-field model for thin-film growth with anisotropic step energy, attachment kinetics, and diffusion, with second-order (thin-interface) corrections. We are mainly interested in the limit in which kinetic anisotropy dominates, and hence we study how the expected shape of a crystallite, which in the long-time limit is the kinetic Wulff shape, is modified by anisotropic diffusion. We present results that prove that anisotropic diffusion plays an important, counterintuitive role in the evolving crystal shape, and we add second-order corrections to the model that provide a significant increase in accuracy for small supersaturations. We also study the effect of different crystal symmetries and discuss the influence of the deposition rate.

DOI: 10.1103/PhysRevE.88.052409 PACS number(s): 68.43.Jk, 81.10.Aj, 81.15.Aa

I. INTRODUCTION

It is well known that epitaxially grown layers in crystalline surfaces can have regular or very complex shapes, ranging from dendritic to fractal (see, e.g., Ref. [1]). There is a plethora of experimental results where crystallites with different shapes are grown on different surfaces by different means [2–8]. These shapes are often puzzling, as some of them appear to be unrelated with the symmetries of the crystallite. It is known that the substrate can play a big role in shaping these crystallites, for instance through the interaction of anisotropic attachment kinetics and anisotropic surface diffusion [2]. The interaction with the substrate can also lead to the formation of three-dimensional (3D) structures, for instance when there is a mismatch between the different crystal structures of the substrate and the crystallite. However, when this mismatch is not too big a two-dimensional model usually suffices to describe the initial stages of growth.

At a large enough scale, it is safe to assume that growth is well described by attachment kinetics on the step edges and by diffusion on the terraces. In this case, we expect that there is a transition from a diffusion-controlled regime for small supersaturation to a kinetics-controlled regime for high values of the supersaturation. Also, in the kinetics-controlled regime, we expect that the shape of the crystallite will be given by Frank's theorem [9], i.e., it will have the kinetic Wulff shape [10,11].

The starting point of the modeling is the classic Burton-Cabrera-Frank (BCF) theory of surface growth [12]. This considers separately the different atomic terraces as domains where the adatoms diffuse, and special conditions apply at the step edges related with attachment kinetics and step energy. Essentially, the crystal surface is considered as a discontinuous system where the boundaries (the step edges) are not fixed but evolving, and growth is controlled by the supersaturation, the only extended variable on the terraces.

Direct numerical simulation of the BCF model implies considerable complexities stemming from its discontinuous nature; the step edges have to be tracked in order to impose the boundary conditions on them, etc. In order to tackle these problems, phase-field techniques have been used in the past, as in Ref. [13] or, in a more comprehensive study, [14], see also Ref. [15] for a thorough study on the stability of epitaxial island growth. These techniques allow, to different extents, the incorporation of attachment kinetics or the step stiffness to the dynamics.

Attachment kinetics are not completely known for most systems, but we will assume quasi-instantaneous attachment for a given symmetry (fourfold or sixfold). As in Ref. [13], we will use a model similar to the one derived in Ref. [16], which is known to have nonlinear kinetics [17], but it is still capable of describing the transition from diffusion- to kinetics-controlled growth, at least qualitatively, e.g., [18].

Diffusion on the terraces has typically been considered isotropic, even though it is well known that diffusion can be anisotropic depending on the symmetries of the surface [19,20]. In some cases, diffusion anisotropy has been measured experimentally [21].

In theoretical studies, diffusion anisotropy has been very rarely studied in connection with step flow until recently [22–24]. Most of the works that deal with diffusion anisotropy in step flow derive equations for the step profile in the quasistatic approximation ($\partial_t c = 0$). Some studies assume alternating anisotropies in the steps [22,25,26] and have found results such as a finite length instability due to the interplay of step stiffness and diffusion anisotropy [25]. In the case of an arbitrary diffusion tensor, the same for all steps, it has been found that the effect of anisotropic diffusion on the step meandering instability [27] is always stabilizing except when the fast diffusion axis is almost perfectly aligned with the step [25]. For review of this line of modeling, see Ref. [28].

Diffusion on a crystalline surface is a very complex process, in which many different competing mechanisms have been observed experimentally, and some have been explained from first principles [29]. The chemical or collective diffusion in general depends on interactions among adatoms, particularly at high coverages. We will not dwell on these complexities. We assume that Fick's law is valid, with a constant effective

*esteban.meca@uci.edu

†vshenoy@seas.upenn.edu

‡lowengrb@math.uci.edu

diffusion tensor. Its specific form is constrained only by the underlying symmetries of the crystal surface.

Here we will consider a phase-field model similar to Refs. [30] and [16] but with anisotropic diffusion. A similar approach was undertaken in Ref. [31] for phase transitions in liquid crystals, but we incorporate the thin-interface asymptotics of Ref. [16] to the model.

In the present work we consider a crystalline surface with a given symmetry and a thin layer that grows by incorporating atoms that are deposited on the surface at a given rate. For simplicity, we do not consider desorption, and therefore the supersaturation at the surface increases approximately linearly with time far from the step edge. This leads to a transition from a diffusion- to a kinetics-controlled regime, which has been studied in the context of dendritic alloy solidification experimentally [32] and numerically using a similar model [18]. In order to compare qualitatively with experimental results, we are mainly interested in the long-time behavior of the system, and therefore we are only partially concerned with the actual transition, which in any case can only be captured qualitatively with the present model.

To summarize, we model the dynamics of a thin-film by using a phase-field formulation that incorporates anisotropic diffusion, anisotropic attachment kinetics, and anisotropic step stiffness, taking into account thin interface corrections. The model, the main assumptions behind it and some of its limitations are described in Sec. II; the numerical techniques used to solve the model are briefly discussed in Sec. III; and finally in Secs. IV and V we present and discuss the results.

II. MODEL

A. Sharp-interface model

The starting point of our modeling is the sharp-interface model, which is basically the BCF theory with small modifications (see Fig. 1). First, local mass conservation leads to the following equation for the concentration of adatoms per unit of surface [33]:

$$\partial_t c = \nabla \cdot (\mathrm{D}\nabla c) + F - \frac{c}{\tau}, \tag{1}$$

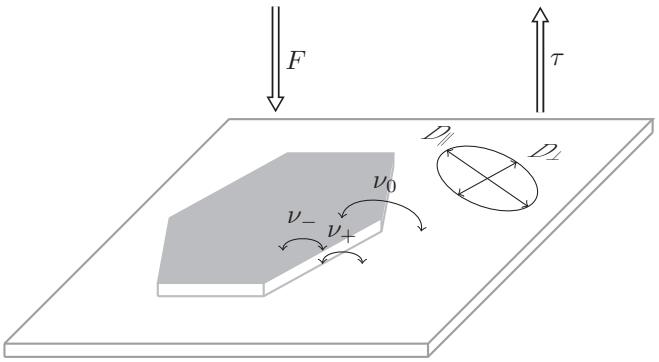

FIG. 1. Diagram of an evolving thin film. We assume that a crystal grows on a terrace where diffusion may be anisotropic diffusion. There are attachment-detachment kinetics from both terraces (ν_+, ν_-) as well as step permeability (ν_0). There is a constant deposition flux F and a desorption time τ.

where D is a diffusion tensor, the second term in the right-hand side corresponds to the rate of deposition of adatoms and the third term models the desorption of adatoms.

We also assume a linearized Gibbs-Thomson relation for the equilibrium concentration at the step edge:

$$c_{\mathrm{eq}} = c^0_{\mathrm{eq}}[1 + \Gamma(\xi_s(\theta) + \xi_s''(\theta))\kappa], \tag{2}$$

where c^0_{eq} is the equilibrium concentration for a flat interface, κ is the curvature of the step, and $\xi_s(\theta) + \xi_s''(\theta)$ is proportional to the step stiffness, with θ being the normal angle. The constant Γ is defined in such a way that, in the absence of anisotropy, $\xi_s(\theta) = 1$.

If we define c_+ (c_-) as the concentration directly ahead (behind) the step edge, mass conservation at the step edge leads to:

$$\mathbf{n} \cdot (\mathrm{D}\nabla c)_+ - \mathbf{n} \cdot (\mathrm{D}\nabla c)_- = \frac{v_n}{\Omega} - v_n(c_+ - c_-), \tag{3}$$

where Ω is the surface occupied by an atom in the solid phase.

Linear phenomenological kinetics imply the following equation [34]:

$$\frac{v_n}{\Omega} = k_+(c_+ - c_{\mathrm{eq}}) + k_-(c_- - c_{\mathrm{eq}}), \tag{4}$$

where the constants $k_\pm$ might depend on the interface orientation.

In the limit of step transparency, that is, high step permeability (see Sec. V and Ref. [14]), we can assume that $c_+ = c_- = c_I$, which leads, by combining Eqs. (3) and (4), to the following boundary conditions at the step edge:

$$c_I = c^0_{\mathrm{eq}} + c^0_{\mathrm{eq}}\Gamma[\xi_s(\theta) + \xi_s''(\theta)]\kappa + \tilde{\beta}(\theta)v_n \tag{5}$$

$$\frac{v_n}{\Omega} = \mathbf{n} \cdot (\mathrm{D}\nabla c)_+ - \mathbf{n} \cdot (\mathrm{D}\nabla c)_-, \tag{6}$$

where $\tilde{\beta}(\theta) = [(k_+ + k_-)\Omega]^{-1}$ is the kinetic coefficient.

It is important to notice that, in this limit, the model is identical with a solidification model and that the asymmetry in the attachment-detachment kinetics (i.e., the Ehrlich-Schwoebel effect) is irrelevant.

Before proceeding further, let us discuss the parametrization of the diffusion tensor. Assuming symmetry, the diffusion tensor can be diagonalized by a rotation:

$$\mathrm{D} = \mathrm{R}(\psi)\begin{pmatrix} D_\parallel & 0 \\ 0 & D_\perp \end{pmatrix}\mathrm{R}(\psi)^{-1}, \tag{7}$$

where $D_\parallel$ denotes the largest eigenvalue of the two (without loss of generality). The angle ψ corresponds to the (counterclockwise) angle that the axes have to be rotated to coincide with the principal diffusion axes. Therefore, the rotation matrix $\mathrm{R}(\psi)$ is given as:

$$\mathrm{R}(\psi) = \begin{pmatrix} \cos\psi & -\sin\psi \\ \sin\psi & \cos\psi \end{pmatrix}. \tag{8}$$

Defining two new parameters:

$$\bar{D} = \frac{1}{2}(D_\parallel + D_\perp); \quad \delta = \frac{D_\parallel - D_\perp}{D_\parallel + D_\perp}, \tag{9}$$

the tensor D can then be written in a compact form as a function of these parameters:

$$\mathrm{D} = \bar{D}\tilde{\mathrm{D}} = \bar{D}\begin{pmatrix} 1+\delta\cos(2\psi) & \delta\sin(2\psi) \\ \delta\sin(2\psi) & 1-\delta\cos(2\psi) \end{pmatrix}. \quad (10)$$

Scaling space with a given characteristic length l (see Sec. III A below) and time with $l^2/\bar{D}$, and defining $u = (c - c^0_{\mathrm{eq}})\Omega$, we obtain the following nondimensional system:

$$\partial_t u = \boldsymbol{\nabla}\cdot(\tilde{\mathrm{D}}\boldsymbol{\nabla}u) + f - \frac{u}{\tau_v}, \quad (11)$$

$$v_n = \mathbf{n}\cdot(\tilde{\mathrm{D}}\boldsymbol{\nabla}u|_+ - \tilde{\mathrm{D}}\boldsymbol{\nabla}u|_-), \quad (12)$$

$$u_I = d_0[\xi_s(\theta) + \xi_s''(\theta)]\kappa + \beta(\theta)v_n, \quad (13)$$

where $\beta(\theta) = \Omega\tilde{\beta}(\theta)\bar{D}/l$, $\tau_v = \tau\bar{D}/l^2$, $d_0 = \Omega\Gamma c^0_{\mathrm{eq}}/l$, and $f = l^2(\Omega/\bar{D})(F - c^0_{\mathrm{eq}}/\tau)$. Also, we define $\beta(\theta) = \beta\,\xi_k(\theta)$, i.e., the product of the kinetic coefficient with the angle-dependent part. As with the step energy, $\xi_k(\theta) = 1$ in the isotropic case. Finally, in the following, we will omit the tilde of the rescaled diffusion tensor.

B. Phase-field model

In order to numerically solve the previous model, we make use of a phase-field model following Karma and Rappel [16]. The starting point is the free energy functional:

$$\mathcal{F}[\phi] = \int\left[\frac{1}{2}\epsilon^2\xi_s(\Theta)^2|\nabla\phi|^2 + f(\phi) - \epsilon\lambda g(\phi)u\right]dV, \quad (14)$$

where ϕ is the phase variable ($\phi = 1$ marks the thin film crystal domain), $f(\phi) = \phi^2(1-\phi)^2/4$, $g(\phi) = \phi^3(10 - 15\phi + 6\phi^2)/120$. The parameter ϵ, assumed small, corresponds to the interface width and λ is a coupling constant with the diffusion field u. As before, ξ_s is related with the change of interfacial energy with the orientation, and depends on the angle Θ, which is defined as $\tan\Theta = \partial_y\phi/\partial_x\phi$. It can be proved that Θ converges to the actual normal angle θ as $\epsilon \to 0$.

The dynamics of the field ϕ ensue from a variational approach:

$$\alpha\tau(\Theta)\epsilon^2\partial_t\phi = -\frac{\delta\mathcal{F}}{\delta\phi}, \quad (15)$$

where $\delta\mathcal{F}/\delta\phi$ is the variational derivative. This results in the following equation

$$\alpha\tau(\Theta)\epsilon^2\partial_t\phi = \epsilon^2\boldsymbol{\nabla}\cdot[\xi_s(\Theta)^2\boldsymbol{\nabla}\phi] - \epsilon^2\partial_x[\xi_s(\Theta)\xi_s'(\Theta)\partial_y\phi] + \epsilon^2\partial_y[\xi_s(\Theta)\xi_s'(\Theta)\partial_x\phi] - f'(\phi) + \epsilon\lambda g'(\phi)u. \quad (16)$$

We see that when ξ_s does not depend on Θ the equation for the phase-field ϕ is the same as the one found in Ref. [16] shifted to $0 \leqslant \phi \leqslant 1$.

We see below how the function $\tau(\Theta)$ in (16) is related with the kinetic attachment anisotropy. In the case of a completely isotropic system, $\tau(\Theta) \to 1$ as $\epsilon \to 0$. Note that we are introducing the different anisotropies as in Ref. [30].

For the diffusion field u we have:

$$\partial_t u = \boldsymbol{\nabla}\cdot(\mathrm{D}\boldsymbol{\nabla}u) + f - \frac{u}{\tau_v} - \partial_t\phi, \quad (17)$$

which is Eq. (11) with an additional coupling term with the phase field.

C. Connection of the phase-field model with the sharp-interface model

In a similar way as in Ref. [16] we have performed a second-order thin-interface expansion in the interface width ϵ to obtain equations (12), (13), and (11) in the limit $\epsilon \to 0$. This expansion is performed in detail in Appendix A. Here we summarize the main results.

To begin with, we recover the Gibbs-Thomson equation (13) and the adatom conservation condition (12) when $\epsilon \to 0$ with the following model parameters as a function of the physical parameters:

$$\lambda = \frac{a_1}{d_0}, \quad (18)$$

$$\alpha = \frac{\beta}{d_0}, \quad (19)$$

where $a_1 = 10\sqrt{2}$.

Also, if we define

$$\tau(\Theta) = \tau_0(\Theta) + \tau_1(\Theta)\epsilon \quad (20)$$

we have that

$$\tau_0(\Theta) = \xi_s(\Theta)\xi_k(\Theta). \quad (21)$$

For the equation to be correct to the next order in ϵ, it is shown in Appendix A that

$$\tau_1(\Theta) = a_2\frac{\xi_s(\Theta)^2}{\beta\{1+\delta\cos[2(\psi-\Theta)]\}}, \quad (22)$$

where $a_2 = 47\sqrt{2}/60$.

Finally, for the kinetic and line energy anisotropies we take the following prescription:

$$\xi_{s,n}(\Theta) = 1 + \epsilon_{s,n}\cos(n\Theta), \quad (23)$$

$$\xi_{k,n}(\Theta) = 1 + \epsilon_{k,n}\cos(n\Theta - n\Theta_0), \quad (24)$$

where Θ_0 can have different values. A usual assumption is $\Theta_0 = \pi/n$, which corresponds to maximal line energy along the directions where the kinetic coefficient is minimal.

III. NUMERICAL METHOD

To solve Eqs. (16) and (17) we use the adaptive nonlinear multigrid algorithm developed by Wise *et al.* [35], and the corresponding solver BSAM. Equations are discretized using finite differences and we use an implicit Crank-Nicolson scheme in time. More details together with a grid adaptation example are shown in Appendix B.

A. Parameters

In Table I we show a summary of the chosen parameters. The interface thickness ϵ has been chosen as small as computationally feasible, see Sec. IV and Appendix B. We use seven levels of mesh refinement, where each refinement corresponds to a halving of the grid spacing; the finest mesh corresponds to $\Delta x = 0.001\,95$. Note that we have used a step energy anisotropy substantially smaller than the kinetic

TABLE I. Parameters used to compute the phase-field constants and to build the anisotropy functions.

Parameter	Symbol	Value
Capillary parameter	d_0	6×10^{-4}
Reference deposition flux	f_0	0.677
Reference kinetic coefficient	β_0	5.54×10^{-3}
Kinetic anisotropy (n-fold)	$\epsilon_{k,n}$	0.08
Step energy anisotropy (n-fold)	$\epsilon_{s,n}$	0.001

anisotropy, which makes the step energy anisotropy essentially irrelevant. This is because we are concerned with the long-term behavior, which we expect will be dominated by kinetics. The competition between the step and kinetic anisotropies has been described elsewhere [36].

The values in Table I are nondimensional and they depend on a given characteristic length l. We pick $l = 1\ \mu$m, consistent with the size of the crystallites in many experiments [4–8] and with the size of our computational domain (see Appendix B). This implies a capillary length of $d_0 = 6 \times 10^{-10}$ m, which is also consistent with the order of magnitude of the step stiffness reported for several materials [37,38].

The remaining parameters, f_0 and β, depend on the surface diffusion coefficient, which in turn depends on the substrate and the value of the temperature T. Its value can vary several orders of magnitude because of that [39–41]. See Sec. V for a discussion on the value of β.

IV. NUMERICAL RESULTS

A. Effect of the second-order correction.

In the following we check the consistency and the convergence of the model, with and without anisotropy. In order to do so we study, first without any anisotropy, the growth of a circular crystal in the presence of an initial supersaturation $u_0 = 0.5$ without a deposition flux. If we extract the radius of the island at a given time for different values of the interface thickness ϵ we obtain the plot in Fig. 2.

From the figure we see that in the studied range of values of the interface thickness the second-order approximation is always closer to the extrapolated value of the radius than the first order model, where $\tau_1 = 0$ instead of Eq. (22).

In Fig. 3 we take the values of the anisotropies given in Table I, with sixfold kinetic anisotropy, and study the shape of a crystallite, which has been grown from an initial small circle, in the absence of supersaturation, but with a constant deposition flux $f = f_0$ and no desorption. We have picked two perpendicular axes of diffusion with the highest (fastest) diffusion axis rotated $\pi/6$ from the x axis, with $D_\parallel = 2D_\perp$ ($\delta = 0.33$). The crystals are shown at time $t = 1.1$ with different choices of ϵ using the first-order method (top) and the second-order method (bottom).

Although the crystal has sixfold symmetry, with dendrites forming in the direction of small kinetic coefficient, there is a strong fourfold component driven by the diffusion anisotropy. In particular, the four prominent dendrites grow in the slow diffusion direction while the dendrites in the fast diffusion direction are suppressed. This effect had been

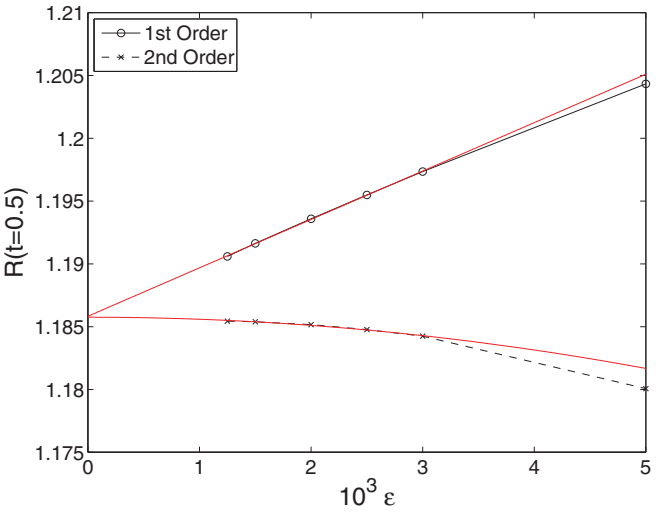

FIG. 2. (Color online) The radius of a circular island at time $t = 0.5$ as a function of the interface thickness ϵ. The island grows due to an initial uniform supersaturation. Results from the first- and second-order schemes are shown, as labeled, together with linear and quadratic fits. The first-order term is obtained by taking $\tau_1 = 0$ in Eq. (20) rather than the form given in Eq. (22). The initial supersaturation is $u_0 = 0.5$, an the kinetic coefficient is $\beta = 4\beta_0$.

observed previously [31], but we see in Fig. 3 how this effect depends strongly on the interface width. For instance we see that for $\epsilon = 0.01$ the first-order shape has already grown small dendrites in the slow diffusion direction, whereas the second-order has a more hexagonal shape. For the second order, as ϵ is decreased small dendrites bud at the vertices of the hexagon, with larger dendrites at the vertices that point away from the fast diffusion direction. For the first order, we see a much more dramatic change, with the dendrites in the fast direction reducing its size and increasing their separation.

A visual inspection shows clearly that the convergence of the second order is much better, with the shape of the crystallite remaining essentially invariant for $\epsilon < 0.005$, but we can quantify how good the convergence is by extracting the perimeters of the crystals and plotting them, similarly to Fig. 2.

The perimeters are plotted in Fig. 4. Clearly, the second-order model behaves much better than the first-order model, converging faster to the extrapolated value for $\epsilon = 0$. The

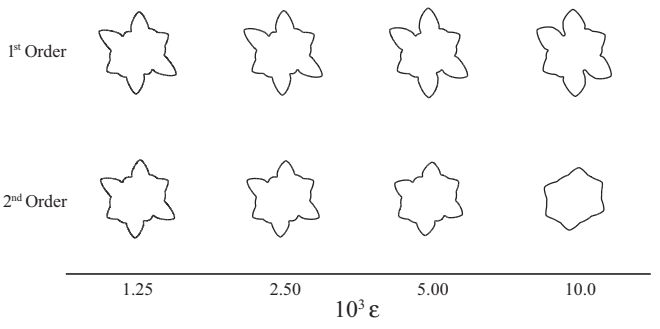

FIG. 3. Snapshots of the evolutions of initially circular crystallites at $t = 1.1$ for different values of ϵ. Top row: first order. Bottom row: second order. $\beta = 4\beta_0$, $f = f_0$, $\psi = \pi/6$ and $\delta = 0.33$.

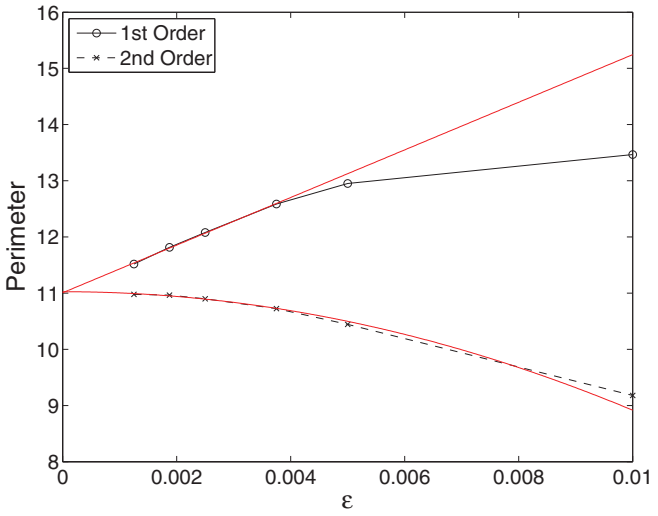

FIG. 4. (Color online) The perimeters of the crystals at $t = 1.1$, for the examples depicted in Fig. 3 for the first- and second-order model formulations, as labeled. The extrapolation is performed using linear and quadratic functions. The kinetic coefficient has the value $\beta = 4\beta_0$, and the deposition flux is $f = f_0$.

extrapolation has been done by fitting a line for the first-order model and a parabola centered at $\epsilon = 0$ for the second-order model.

Finally, it should be noted that both in Figs. 2 and 4 the extraction of the radius and the perimeter is greatly hindered by grid anisotropy, and many levels of refinement are required to obtain a good convergence. Grid anisotropy is a well-known effect and sometimes can be quantified [16], but in our case the convergence analysis in Figs. 2 and 4 helped us select the right number of refinements and the right value of the interface width ϵ to obtain accurate results.

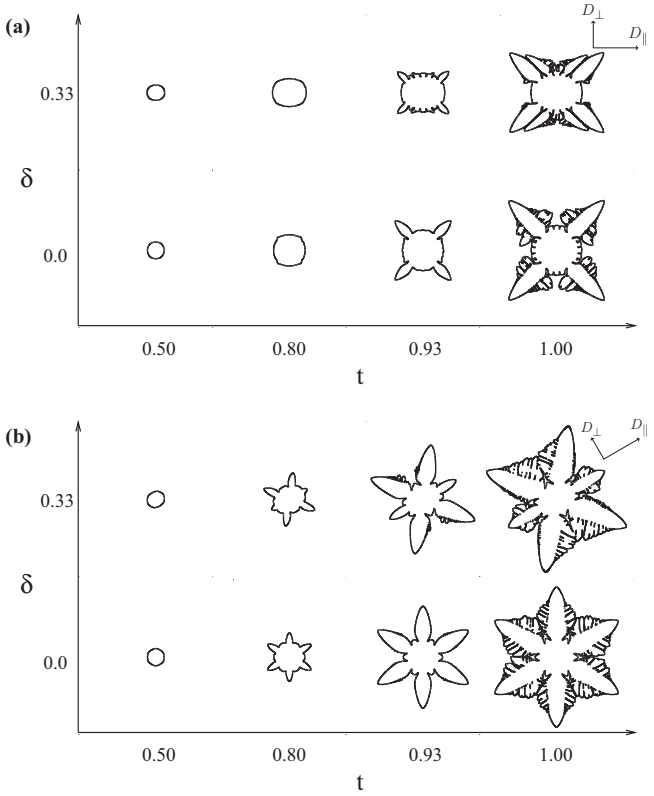

FIG. 5. Evolution of selected cases with $\delta = 0$ and $\delta = 0.33$. In (a), the fourfold kinetic anisotropy case is shown while in (b) the sixfold case is shown. The deposition flux is $f = 1.0$ and the kinetic coefficient is $\beta = \beta_0$. The diffusion tensor rotation angle is $\psi = 0$ for the fourfold case and $\psi = \pi/6$ for the sixfold. There is a small line energy anisotropy, $\epsilon_{s,6} = 0.001$ and the kinetic anisotropy has a strength $\epsilon_{k,n} = 0.08$, the interface thickness is $\epsilon = 0.001\,25$ in the fourfold case and $\epsilon = 0.0025$ in the sixfold case.

B. Effect of anisotropic diffusion

In this section, we study the shapes of a crystallite for different values of the anisotropic diffusion parameter δ, and for fourfold and sixfold kinetic anisotropy. The fact that we are ignoring desorption means that the value of the supersaturation far away from the interface will be growing following an approximately linear law.

We start describing the time evolution in two extreme cases, one corresponds to isotropic diffusion ($\delta = 0$) and the other corresponds to a strongly anisotropic diffusion, $D_\parallel = 2D_\perp$ ($\delta = 0.33$). The crystal evolutions are shown in Fig. 5 where the fourfold symmetric case is shown in Fig. 5(a) and the sixfold symmetric case is shown in Fig. 5(b). In Fig. 5(a), the principal diffusion axes are not rotated while in Fig. 5(b), the axes are rotated by $\pi/6$. In this and in the subsequent examples, the initial condition is a small circular island with radius $r = 0.3$ and zero supersaturation everywhere.

At short times (e.g., $t = 0.50$), the crystal is circular when $\delta = 0$ (isotropic diffusion) but when $\delta = 0.33$ (anisotropic diffusion), the crystal shape is ellipselike, where the major axis points in the direction of fast diffusion.

By $t = 0.80$ the crystal has more than doubled its area, and in the sixfold case we see the dendrites budding in the directions in which the kinetic coefficient is the smallest. Recall that the value of the surface energy anisotropy is small and hence we do not see interactions between the surface and kinetic anisotropies. Note the difference among the two symmetries, in the fourfold case the dendrites take longer to form.

By $t = 0.93$ there is a dramatic change in the evolution. To begin with, we observe that the timescale of the evolution has changed, as now it is much faster. We see that some dendrites have developed from the original buds, and side branches have begun to form. When diffusion is isotropic, the crystals take on symmetric shapes. When the diffusion is anisotropic, dendrites in the slow diffusion directions are suppressed, as can be seen in the sixfold case. Further, side branches begin to form in the slow-diffusion directions.

Finally, by $t = 1.0$, the dendrites and side branches have grown significantly to the point where the dendrites are nearly merging. A difference is clearly seen between the sixfold and the fourfold case. In the sixfold case, the number of dendrites is constant even when δ is high, while in the fourfold case, secondary dendrites appear, leading to a competition between primary and secondary dendrites. These secondary dendrites compete with the primary dendrites and also exhibit the formation of side branches.

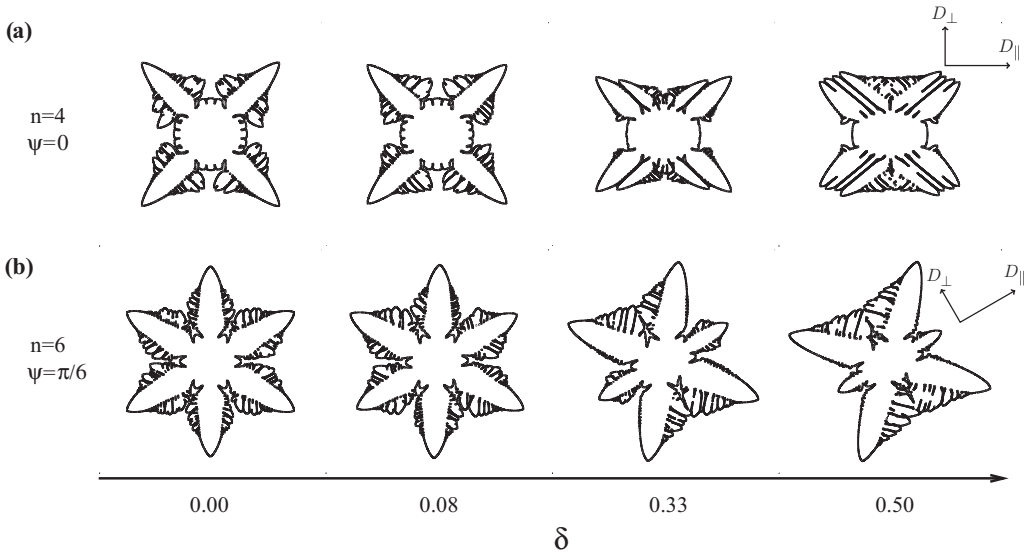

FIG. 6. Summary of the shapes of crystals of comparable size with a fourfold kinetic anisotropy (a) and a sixfold kinetic anisotropy (b), for different values of the diffusion anisotropy parameter δ. There is a small line energy anisotropy, $\epsilon_{s,6} = 0.001$, the kinetic anisotropy has a strength $\epsilon_{k,n} = 0.08$, the deposition rate is $f = 1.0$, and the kinetic coefficient is $\beta = \beta_0$. The interface thickness has a value $\epsilon = 0.0025$ for the sixfold case and $\epsilon = 0.001\,25$ for the fourfold.

To elucidate the dynamics further, we perform an additional study of the growth shapes as a function of the parameter δ. In addition to the cases with $\delta = 0$ and $\delta = 0.33$, we consider two more cases with $\delta = 0.08$ and $\delta = 0.5$, which correspond to $D_\parallel/D_\perp = 1.17$ and 3, respectively. The results are shown in Figs. 6(a) and 6(b), where the crystals are shown at times for which they have approximately the same size.

When $\delta = 0$ we observe regular shapes, approximately symmetric with respect to a rotation with the appropriate angle. The dendrites develop in the small kinetic coefficient direction, and this is also true for sidebranching, which develops at $\pi/2$ from the dendrite direction in the fourfold case and $\pi/3$ in the sixfold case.

When $\delta = 0.08$ the crystallite largely retains the $\delta = 0$ shape, but the (approximate) rotational symmetry is lost. This is clearly seen in the way in which sidebranching is less developed in the fast diffusion direction, even more so in the sixfold case, where even the dendrites in the fast diffusion direction (which makes an angle of $\pi/6$ with the horizontal) are clearly smaller.

In the $\delta = 0.33$ case, there is a clear divide between the fourfold and the sixfold crystals, already seen in Fig. 5. For this value of the undercooling, sidebranching does not develop in the fast diffusion direction, and in the sixfold case the growth of the dendrites in that direction is greatly diminished. Also in the sixfold case, we observe how the dendrites closer to the slow diffusion direction tend to diverge, i.e., they form an angle greater than $\pi/3$.

While in the sixfold case the number of dendrites is always the same, we observe that in the fourfold case there are more dendrites when δ (and time) increases, with a spacing that is smaller the closer the dendrites are to the slow diffusion direction. This signals a diffusion-limited instability, such as the Mullins-Sekerka instability [42], where the number of dendrites (fingers) increases in time and competition ensues between the dendrites.

In the most anisotropic case, $\delta = 0.50$, all the trends that were observed for $\delta = 0.33$ are confirmed. For both symmetries, there is almost no sidebranching in the fast diffusion direction. In the fourfold case, there are more dendrites and their spacing has been decreased. In the sixfold case, the dendrites in the fast diffusion direction are quite small, with the remaining dendrites separated by an angle of almost $\pi/2$, leading to a quasifourfold crystallite.

Finally, we consider variations in the direction of the principal diffusion axes. In the fourfold case we have considered so far that the principal axes of diffusion are in the directions of maximum kinetic coefficient. We now change this by rotating the diffusion tensor by $\psi = \pi/4$. In the sixfold case we have considered the case in which the fast diffusion is along the minimum kinetic coefficient direction, now we will assume the opposite and take $\psi = 0$. The results are shown in Fig. 7.

The first thing that we notice in Fig. 7 is that the shapes of the crystals are completely different when we change the axes of diffusion. In Fig. 7(a), the fourfold case when $\psi = \pi/4$, we observe that we do not have a flattened hourglass shape, like in Fig. 7(b), the case when $\psi = 0$, but rather the slow diffusion directions coincide with one pair of dendrites, which become much more elongated, while the remaining dendrites are significantly suppressed giving this crystal a highly distorted quasitwofold symmetry shape.

In Fig. 7(c), the sixfold case with $\psi = 0$, we also observe that the dendrites in the slow diffusion direction are more developed, while the others are smaller and have nearly equal sizes. This results eventually in a distorted star polygon at later times.

Let us note that in Fig. 7 we have used a larger value of f and shown the results at an earlier time than in Figs. 5 and 6. This is why the dendrites are wider than in the previous cases.

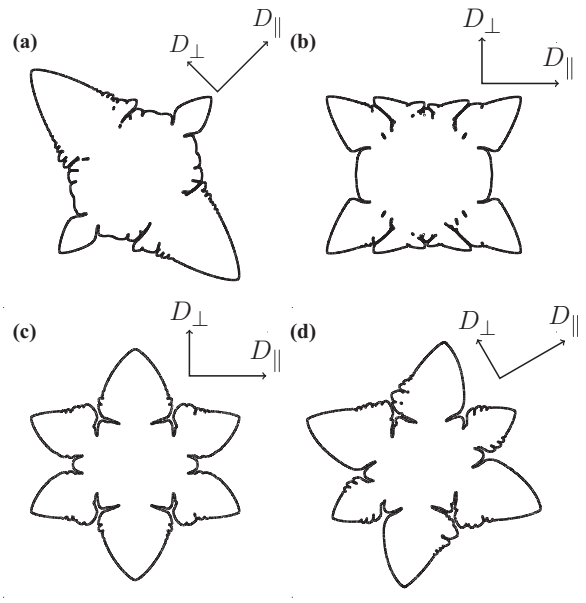

FIG. 7. Effect of different principal directions of diffusion, for the $f = 4f_0$, $\delta = 0.33$, and $\beta = \beta_0$ case. (a) fourfold kinetics with $\psi = \pi/4$. (b) fourfold kinetics with $\psi = 0$. (c) sixfold kinetics with $\psi = 0$. (d) sixfold kinetics with $\psi = \pi/6$. The anisotropies and the different values of the interface thickness are the same as in Figs. 5 and 6.

V. DISCUSSION

In this paper we have developed the simplest phase-field model that incorporates kinetic anisotropy, step energy anisotropy, and diffusion anisotropy, correct to second order in the thin-interface asymptotics. The analysis in Appendix A leads to an additional term in Eq. (16), the τ_1 term in Eq. (20), which has the form given in Eq. (22). It is one of our main results that this term is presented in this form.

We have undertaken a study of the different shapes of crystallites on a crystalline surface, and the influence of the degree of anisotropic diffusion, for different symmetries, e.g., by considering sixfold and fourfold anisotropic kinetic coefficients.

In the fourfold case we have found an interesting interaction of anisotropic diffusion with kinetic anisotropy, exemplified in a transition, as the diffusion anisotropy strength δ is increased, from a regime in which the crystal grows as sidebranches form along the primary dendrites (i.e., the dendrites along the direction of small kinetic coefficient) to a different regime where growth occurs through a competition among the dendrites in the slow diffusion directions, as shown in Fig. 6. It is also noteworthy that this transition is absent in the sixfold case, possibly due to the earlier development of the dendrites (cf. Fig. 5).

The main effect of the increased value of δ in the sixfold case is the suppression of dendrites in the fast diffusion direction, see Fig. 6. This effect has already been reported for a similar model for liquid crystals [31] and for step-profile equations in the quasistatic limit [24]. It reflects a preference of dendritic growth in the direction where lateral diffusion is the fastest. This effect is not restricted to the the sixfold case, as it can be seen in Fig. 7 for the fourfold case when the principal diffusion axes are rotated by $\psi = \pi/4$.

The remaining dendrites tend to separate as much as possible from each other. In Fig. 6 with $\delta = 0.5$, for example, the competition between the kinetic and diffusional anisotropies leads to a quasifourfold symmetric crystal from sixfold kinetics. Nevertheless, a telltale sign that the crystal shown in Fig. 6 (with sixfold kinetic anisotropy and $\delta = 0.5$) is not fourfold symmetric is the preferred development of side branches in the slow diffusion direction, which is consistent with a diffusion-limited instability.

Another feature that is present in the results is a relationship between the supersaturation and the tip radius of the dendrites. This is seen in Fig. 5 where the curvature of the dendrites at the tip decreases with increasing time (and therefore supersaturation), hence the radius of curvature ρ increases. Since the velocity of the front also increases with the supersaturation, as can be seen on the same figure, we conclude that the dendrites are away from the regime that is most commonly treated in the literature, i.e., $\rho^2 V \approx$ const. This has been noticed and characterized previously in Ref. [18] for a similar model in the context of solidification of pure substances, and alternative scaling laws were proposed.

In our numerical simulations, we have tried to limit the influence of numerical grid anisotropy on the results by taking the interface thickness small and using a highly refined adaptive mesh. Because the adaptive mesh is not isotropic [43], numerical noise generates small asymmetries in the crystallites, which are perhaps most noticeable when $\delta = 0$ and the kinetic anisotropy is sixfold symmetric. The numerically generated anisotropies are much smaller than the diffusion anisotropy, even in the case when $\delta = 0.08$, and thus we are confident that the effects of diffusion anisotropy are being accurately captured.

The phase-field model we have used here is known to have very nonlinear kinetics in the high supersaturation regime. This has been recognized and discussed in the past, together with possible modifications of the model [17,44]. Further, the coalescence of side branches (and dendrites) is handled phenomenologically in the phase-field approach and depends on the interface thickness. Nevertheless, by simulating crystals with different interface thicknesses, using highly refined adaptive grids, we believe that the transitions in crystallite growth we observed here from anisotropic-diffusion-dominated to kinetics-dominated regimes are characteristic of other related phase-field models [18] and are qualitatively independent of the interface thickness.

The sharp interface model on which this analysis is based has also several limitations. To begin with, we have picked arbitrary periodic functions for the anisotropy functions. This is a standard practice [30] and can be justified assuming that the value of the anisotropy is small enough. For the diffusion anisotropy, the description is more natural, but still our model is limited to the case where the diffusivity tensor is the same in both terraces. This is not necessarily the case in reality [25], but the computation of thin-interface corrections with arbitrary diffusivities at both sides of the interface is an open problem [45,46]. In any case, even considering symmetric but anisotropic diffusivities we uncover a very rich phenomenology.

Finally, the same comment applies to the fact that we have adopted the step transparency approximation [14,47], which makes the Ehrlich-Schwoebel effect (kinetic attachment-detachment asymmetry) irrelevant in this limit. Transparency, i.e., a high degree of step permeability, is a strong assumption, and one of its consequences is nonlocal dynamics, as adatoms are able to diffuse through many steps. Nevertheless, this effect has been observed experimentally in different vicinal surfaces of Si, under different experimental conditions [48,49]. The applicability of the transparency approximation has been discussed by Stoyanov and Tonchev [50]. Their condition for transparency translates in our case to $\beta l/\sqrt{\Omega} \gg 1$, which implies $\beta \gg 10^{-4}$, and hence we are in the region of applicability of the approximation by the argument in Ref. [50]. In any case, the nonlocality is not important as we study a single step, and the kinetics of the model are qualitative in any case. For a recent study of the connection of the kinetic coefficients with microscopic dynamics, including step permeability, see, e.g., Ref. [51].

In conclusion, despite its limitations, this model is capable of uncovering a qualitative picture of how a thin layer of material deposited on a crystalline surface is shaped by different sources of anisotropy.

ACKNOWLEDGMENTS

E.M. acknowledges partial support from the Balsells Foundation. E.M. and J.L. acknowledge partial support from the NSF Division of Mathematical Sciences through Grant No. DMS-1217303. V.S. acknowledges partial support from Grant No. DMS-1216801.

APPENDIX A: ASYMPTOTIC EXPANSION

Here we deduce the findings outlined in Sec. II C. The starting point is Eqs. (16) and (17) for ϕ and u.

1. Curvilinear coordinates

Here we write Eqs. (16) and (17) in the frame of reference of the advancing solidification front, with coordinates adapted to the edge of the growing layer.

a. Anisotropic phase-field equation in curvilinear coordinates

We define a curvilinear coordinate system based on the evolving interface. The coordinates of the interface are given by $[X(s,t),Y(s,t)]$, a function of the arclength s and time t. We introduce an additional coordinate, the normal distance to the interface r, where the normal is given by $\mathbf{n} = [Y'(s,t), -X'(s,t)]$, where the primes denote derivatives over s.

With these definitions, the change of coordinates is given by:

$$x = X(s,t) + rY'(s,t), \tag{A1}$$

$$y = Y(s,t) - rX'(s,t). \tag{A2}$$

In these coordinates, the Jacobian can be easily computed, as well as the gradient. For example,

$$\partial_r \phi = Y' \partial_x \phi - X' \partial_y \phi, \tag{A3}$$

$$\partial_s \phi = (X' + rY'')\partial_x \phi + (Y' - rX'')\partial_y \phi \tag{A4}$$

and inverting the Jacobian, we obtain

$$\begin{aligned} h\partial_x \phi &= (Y' - rX'')\partial_r \phi + X' \partial_s \phi, \\ h\partial_y \phi &= -(X' + rY'')\partial_r \phi + Y' \partial_s \phi, \end{aligned} \tag{A5}$$

where

$$h = X'^2 + Y'^2 + r(X'Y'' - Y'X'') = 1 + r\mathcal{K} \tag{A6}$$

is the determinant of the Jacobian, with $\mathcal{K}$ being the curvature of the interface.

With this notation, the gradient can be written in the following form:

$$\nabla \phi = \partial_r \phi \, \mathbf{r} + \frac{1}{h} \partial_s \phi \, \mathbf{s} \tag{A7}$$

with $\mathbf{r}$ being the normal vector to the interface and $\mathbf{s}$ the tangent vector.

With the previous definitions it readily follows that

$$\tan\Theta = \frac{\partial_y \phi}{\partial_x \phi} = \frac{-(X' + rY'')\partial_r \phi + Y' \partial_s \phi}{(Y' - rX'')\partial_r \phi + X' \partial_s \phi}. \tag{A8}$$

After a lengthy calculation it can be seen that the functional derivative of $\mathcal{F}$ from Eq. (14) can be written as

$$\begin{aligned} \frac{\delta \mathcal{F}}{\delta \phi}[\phi] = -\frac{\epsilon^2}{1 + r\mathcal{K}} \Bigg\{ & \partial_r [(1 + r\mathcal{K})\xi_s(\Theta)^2 \partial_r \phi] \\ & + \partial_s \left[\frac{\xi_s(\Theta)^2 \partial_s \phi}{1 + r\mathcal{K}} \right] + \partial_s [\xi_s(\Theta)\xi_s'(\Theta)\partial_r \phi] \\ & - \partial_r [\xi_s(\Theta)\xi_s'(\Theta)\partial_s \phi] \Bigg\} + f'(\phi) - \epsilon\lambda g'(\phi) u \end{aligned} \tag{A9}$$

With this change of coordinates, the time derivative becomes

$$\begin{aligned} \partial_t \tilde{\phi}(t,r,s) &= \partial_t \phi(t, X + rY', Y - rX')|_{r,s \text{ const.}} \\ &= \partial_t \phi + \partial_x \phi(\dot{X} + r\dot{Y}') + \partial_y \phi(\dot{Y} - r\dot{X}'), \end{aligned} \tag{A10}$$

where the dot denotes a time derivative, and $\tilde{\phi}$ stands for the function in the new variables.

By using (A5), we can find, after some algebra:

$$\partial_t \phi = \partial_t \tilde{\phi} - v_n \partial_r \tilde{\phi} - v_t \partial_s \tilde{\phi} + r \frac{v_n'}{1 + r\mathcal{K}} \partial_s \tilde{\phi}, \tag{A11}$$

where $v_n = Y'\dot{X} - X'\dot{Y}$ and $v_t = X'\dot{X} + Y'\dot{Y}$ are the normal and tangential interface velocities, respectively. Note that Eq. (A11) is exact and not a small r approximation.

Finally, we can put together Eqs. (A11) and (A9) after dropping the tildes:

$$\begin{aligned} & \alpha\, \tau(\Theta)\epsilon^2 \left(\partial_t \phi - v_n \partial_r \phi - v_t \partial_s \phi + r \frac{v_n'}{1 + r\mathcal{K}} \partial_s \phi \right) \\ & = \frac{\epsilon^2}{1 + r\mathcal{K}} \Bigg\{ \partial_r [(1 + r\mathcal{K})\xi_s(\Theta)^2 \partial_r \phi] + \partial_s \left[\frac{\xi_s(\Theta)^2 \partial_s \phi}{1 + r\mathcal{K}} \right] \\ & \quad + \partial_s [\xi_s(\Theta)\xi_s'(\Theta)\partial_r \phi] - \partial_r [\xi_s(\Theta)\xi_s'(\Theta)\partial_s \phi] \Bigg\} \\ & \quad - f'(\phi) + \epsilon\lambda g'(\phi) u \end{aligned} \tag{A12}$$

b. Anisotropic diffusion in curvilinear coordinates

Just like the phase-field equation, we need to express the anisotropic diffusion equation (17) in curvilinear coordinates.

To do so we need first to find the divergence of the diffusion tensor applied to the gradient of the u field. The gradient is computed as in Appendix A1a,

$$\boldsymbol{\nabla} u = \partial_r u\, \mathbf{r} + \frac{1}{h}\partial_s u\, \mathbf{s}. \tag{A13}$$

We need to put the tensor D in curvilinear coordinates too, which means that its components depend on s due to the transformation:

$$\begin{aligned}\mathrm{D} &= \mathrm{R}(\theta)^{-1}\mathrm{R}(\psi)\begin{pmatrix} D_{\parallel} & 0 \\ 0 & D_{\perp}\end{pmatrix}\mathrm{R}(\psi)^{-1}\mathrm{R}(\theta) \\ &= \begin{pmatrix} D_{nn} & D_{nt} \\ D_{nt} & D_{tt}\end{pmatrix}.\end{aligned} \tag{A14}$$

Note that the elements of the matrix depend on s through $\theta = \theta(s)$.

In these coordinates, the divergence of a field $\mathbf{v}$ can be computed as follows:

$$\boldsymbol{\nabla}\cdot\mathbf{v} = \frac{1}{h}\left[\partial_r(v_r h) + \partial_s\left(\frac{v_s}{h}\right)\right] = \frac{1}{h}[\partial_r(v^r h) + \partial_s(v^s h)], \tag{A15}$$

where r, s subscripts or superscripts of v are coordinate indices, they do not denote derivatives. Since we are using unit vectors, the s component should be divided by h to extract the contravariant component. Then, we have the following:

$$\begin{aligned}\boldsymbol{\nabla}\cdot(\mathrm{D}\boldsymbol{\nabla} u) = {}& \frac{1}{h}\partial_r(h D_{nn}\partial_r u + D_{nt}\partial_s u) \\ & + \frac{1}{h}\partial_s\left(D_{nt}\partial_r u + \frac{1}{h}D_{tt}\partial_s u\right).\end{aligned} \tag{A16}$$

2. Asymptotics: outer expansion

Here we find the equations satisfied by the fields in the outer expansion, which is valid far away from the interface, as given here:

$$\tilde{\phi}(r,s) = \tilde{\phi}_0 + \tilde{\phi}_1 + \epsilon^2\tilde{\phi}_2 + \cdots \tag{A17}$$

$$\tilde{u}(r,s) = \tilde{u}_0 + \epsilon\tilde{u}_1 + \epsilon^2\tilde{u}_2 + \cdots. \tag{A18}$$

For $\tilde{u}$ it is trivially found that the (anisotropic) BCF equation holds at all orders:

$$\partial_t\tilde{u}_k = \boldsymbol{\nabla}\cdot(\mathrm{D}\boldsymbol{\nabla}\tilde{u}_k) + f - \frac{\tilde{u}_k}{\tau_v}. \tag{A19}$$

The phase-field variable $\tilde{\phi}$ is simply 1 or 0 and distinguishes between the upper and lower steps.

For future use, we compute here the limit of Eq. (A19) as $r \to 0^{\pm}$ in curvilinear coordinates. From Appendix A1a the equation can be written in this limit as follows:

$$\begin{aligned}&\partial_t\tilde{u}_k|^{\pm} - v_n\partial_r\tilde{u}_k|^{\pm} - v_t\partial_s\tilde{u}_k|^{\pm} \\ &\quad = \boldsymbol{\nabla}\cdot(\mathrm{D}\boldsymbol{\nabla}\tilde{u}_k)|^{\pm} + f - \frac{\tilde{u}_k|^{\pm}}{\tau_v}.\end{aligned} \tag{A20}$$

To find the form of the anisotropic Laplacian in this case we use the results of Appendix A1b. By using the following identities:

$$\partial_s D = \partial_\theta D\mathcal{K}, \tag{A21}$$

$$\partial_s h = r\mathcal{K}\partial_\theta\mathcal{K} \tag{A22}$$

and also the following relations, that are readily deduced from the definitions of the elements of the diffusion tensor:

$$\partial_\theta D_{nt} = D_{tt} - D_{nn}, \tag{A23}$$

$$\partial_\theta D_{tt} = -2D_{nt} \tag{A24}$$

we finally find, after some algebra, the expression of the anisotropic Laplacian on the interface:

$$\begin{aligned}\boldsymbol{\nabla}\cdot(\mathrm{D}\boldsymbol{\nabla}\tilde{u}_k)|^{\pm} = {}& D_{tt}\mathcal{K}\partial_r\tilde{u}_k|^{\pm} + D_{nn}\partial_r^2\tilde{u}_k|^{\pm} + 2D_{nt}\partial_r\partial_s\tilde{u}_k|^{\pm} \\ & + D_{tt}\partial_s^2\tilde{u}_k|^{\pm} - 2D_{nt}\mathcal{K}\partial_s\tilde{u}_k|^{\pm}.\end{aligned} \tag{A25}$$

The previous relation means that

$$\begin{aligned}&\partial_t\tilde{u}_k|^{\pm} - v_t\partial_s\tilde{u}_k|^{\pm} - f + \frac{\tilde{u}_k|^{\pm}}{\tau_v} - D_{tt}\partial_s^2\tilde{u}_k|^{\pm} + 2D_{nt}\mathcal{K}\partial_s\tilde{u}_k|^{\pm} \\ &\quad = (v_n + D_{tt}\mathcal{K})\partial_r\tilde{u}_k|^{\pm} + D_{nn}\partial_r^2\tilde{u}_k|^{\pm} + 2D_{nt}\partial_r\partial_s\tilde{u}_k|^{\pm}\end{aligned} \tag{A26}$$

for all $k \geqslant 0$.

3. Asymptotics: inner expansion and matching

Near the interface, we make the transformation $\eta = r/\epsilon$ and expand the two fields as follows:

$$\Phi(\eta,s) = \Phi_0 + \epsilon\Phi_1 + \epsilon^2\Phi_2 + \cdots \tag{A27a}$$

$$U(\eta,s) = U_0 + \epsilon U_1 + \epsilon^2 U_2 + \cdots. \tag{A27b}$$

When written in curvilinear coordinates, Eq. (16) takes the form given in Appendix A1a. If we expand Eq. (A12) to second order in ϵ, we obtain the following:

$$\begin{aligned}&-\alpha(\epsilon\tau_0(\theta)v_n\partial_\eta\Phi + \epsilon^2\{v_n\tau_1(\theta)\partial_\eta\Phi \\ &\quad + [(v_n + v_t)\tau_0(\theta) + v_n\tau_0'(\theta)]\partial_s\Phi - \tau_0(\theta)\partial_t\Phi\}) \\ &\quad = \xi_s(\theta)^2\partial_\eta^2\Phi - f'(\Phi) + \epsilon\,\lambda g'(\Phi)U + \epsilon\{\xi_s(\theta)^2\mathcal{K}\partial_\eta\Phi \\ &\qquad + \xi_s(\theta)\xi_s'(\theta)\partial_\eta\partial_s\Phi + \partial_s[\xi_s(\theta)\xi_s'(\theta)\partial_\eta\Phi]\} \\ &\qquad + \epsilon^2(\partial_s\{[\xi_s(\theta)^2 + \xi_s'(\theta)^2 + \xi_s(\theta)\xi_s''(\theta)]\partial_s\Phi\} \\ &\qquad - \eta\mathcal{K}\{\partial_\eta[\xi_s(\theta)\xi_s'(\theta)\partial_s\Phi] + \partial_s[\xi_s(\theta)\xi_s'(\theta)\partial_\eta\Phi]\} \\ &\qquad - \eta\mathcal{K}^2\xi_s(\theta)^2\partial_\eta\Phi)\end{aligned} \tag{A28}$$

For the anisotropic diffusion equation (17), from Eq. (A16) of Appendix A1b, we have that (after making the change and expanding up to order ϵ^0)

$$\begin{aligned}\boldsymbol{\nabla}\cdot(\mathrm{D}\boldsymbol{\nabla} u) \approx {}& \frac{1}{\epsilon^2}D_{nn}\partial_\eta^2 U + \frac{1}{\epsilon}(D_{tt}\mathcal{K}\partial_\eta U + 2D_{nt}\partial_\eta\partial_s U) \\ & + D_{tt}\partial_s^2 U - \eta D_{tt}\mathcal{K}^2\partial_\eta U \\ & - 2D_{nt}\mathcal{K}(\partial_s U + \eta\,\partial_\eta\partial_s U),\end{aligned} \tag{A29}$$

where we have taken into account the properties of the (s-dependent) elements of the diffusion tensor.

With the previous approximation, we can now write Eq. (17) to order zero as:

$$
\begin{aligned}
&-\frac{v_n}{\epsilon}\partial_\eta U + \partial_t U - v_t \partial_s U \\
&= \frac{1}{\epsilon^2} D_{nn}\partial_\eta^2 U + \frac{1}{\epsilon}(D_{tt}\mathcal{K}\partial_\eta U + 2D_{nt}\partial_\eta\partial_s U) \\
&\quad + D_{tt}\partial_s^2 U - \eta D_{tt}\mathcal{K}^2\partial_\eta U - 2D_{nt}\mathcal{K}(\partial_s U + \eta\,\partial_\eta\partial_s U) \\
&\quad + f - \frac{U}{\tau_v} + \frac{v_n}{\epsilon}\partial_\eta\Phi - \partial_t\Phi + v_t\partial_s\Phi. \qquad \text{(A30)}
\end{aligned}
$$

Now, as usual, we introduce the expansion (A27) in (A28) and (A30) and proceed order by order.

a. Order 0

From (A28), collecting terms of order ϵ^0:

$$\xi_s(\theta)^2\partial_\eta^2\Phi_0 - f'(\Phi_0) = 0, \qquad \text{(A31)}$$

which implies, as usual (making use of the fact that Φ is one or zero far from the interface):

$$\tfrac{1}{2}\xi_s(\theta)^2(\partial_\eta\Phi_0)^2 - f(\Phi_0) = 0. \qquad \text{(A32)}$$

Therefore, locating the interface at $\Phi_0 = 1/2$,

$$\eta = \pm\int_{\frac{1}{2}}^{\Phi_0(\eta)} d\Phi \frac{\xi_s(\theta)}{\sqrt{2f(\Phi)}}. \qquad \text{(A33)}$$

For $f(\Phi) = \Phi^2(1-\Phi)^2/4$ we obtain

$$\Phi_0(\eta) = \frac{1}{2}\left[1 \pm \tanh\left(\frac{\eta}{2\xi_s(\theta)\sqrt{2}}\right)\right]. \qquad \text{(A34)}$$

We choose the minus sign, meaning that $\partial_\eta\Phi_0$ will be negative. The other choice would give the same equations, if we assume that ξ depends on $\tan\Theta$, but with a receding interface.

From (A30), collecting terms of the lowest order (ϵ^{-2}), we obtain the following:

$$D_{nn}\partial_\eta^2 U_0 = 0. \qquad \text{(A35)}$$

The only solution that is physically acceptable is $U_0 = \bar{U}_0(s)$, a constant dependent on s. Otherwise it would be impossible to match the inner and outer solutions.

b. Order 1

To first order, the phase-field equation reads as follows:

$$
\begin{aligned}
&\xi_s(\theta)^2\partial_\eta^2\Phi_1 - f''(\Phi_0)\Phi_1 \\
&\quad = -\alpha\tau_0(\theta)v_n\partial_\eta\Phi_0 - \xi_s(\theta)^2\mathcal{K}\partial_\eta\Phi_0 - \xi_s(\theta)\xi_s'(\theta)\partial_\eta\partial_s\Phi_0 \\
&\qquad - \partial_s[\xi_s(\theta)\xi_s'(\theta)\partial_\eta\Phi_0] - \lambda g'(\Phi_0)U_0. \qquad \text{(A36)}
\end{aligned}
$$

Note that this equation has the form $\mathcal{L}\Phi_1 = \mathcal{G}_1$, where the operator $\mathcal{L}$ is self-adjoint. Also, observe that $\mathcal{L}$ is an even operator, i.e., it does not change with the transformation $\eta \to -\eta$. For future use note that ∂_s does not change the evenness while ∂_η changes it.

Now, it is easy to prove the adjoint homogeneous problem $\mathcal{L}\Phi_1 = 0$ (the operator is self-adjoint) has the solution $\Phi_1 = \partial_\eta\Phi_0$, as the previous equation becomes the η derivative of (A31). Thus, the right-hand side of (A36) must be orthogonal to $\partial_\eta\Phi_0$:

$$
\begin{aligned}
&\{\alpha v_n\tau_0(\theta) + \xi_s(\theta)[\xi_s(\theta) + \xi_s''(\theta)]\mathcal{K}\}\int_{-\infty}^{\infty} d\eta(\partial_\eta\Phi_0)^2 \\
&\quad + \lambda U_0\int_{-\infty}^{\infty} d\eta\,\partial_\eta\Phi_0\, g'(\Phi_0) = 0. \qquad \text{(A37)}
\end{aligned}
$$

To obtain the previous equation we have made use of the relation:

$$\partial_s\Phi_0 = -\eta\frac{\xi_s'(\theta)}{\xi_s(\theta)}\mathcal{K}\partial_\eta\Phi_0, \qquad \text{(A38)}$$

obtained from Eq. (A33). Note that the previous equation implies that, even if Φ_0 does not have a definite parity, $\partial_s\Phi_0$ is odd. After some algebra and an integration by parts, we arrive at Eq. (A37).

For the diffusion equation, we obtain the following:

$$D_{nn}\partial_\eta^2 U_1 + v_n\partial_\eta\Phi_0 = 0, \qquad \text{(A39)}$$

which gives, after two integrations:

$$U_1 = \bar{U}_1 + \frac{A}{D_{nn}}\eta - \frac{v_n}{D_{nn}}\int_0^\eta d\eta'\Phi_0(\eta'), \qquad \text{(A40)}$$

where all constants depend on s.

c. Order 2

The phase-field equation at the second order takes the following form:

$$
\begin{aligned}
&-\alpha\left(\tau_0(\theta)v_n\partial_\eta\Phi_1 + \left\{v_n\tau_1(\theta) - \eta\frac{\xi_s'(\theta)}{\xi_s(\theta)}\mathcal{K}[(v_n+v_t)\tau_0(\theta) + v_n\tau_0'(\theta)]\right\}\partial_\eta\Phi_0\right) \\
&= \xi_s(\theta)^2\partial_\eta^2\Phi_2 - f''(\Phi_0)\Phi_2 - \frac{1}{2}\Phi_1^2 f'''(\Phi_0) + \xi_s(\theta)^2\mathcal{K}\partial_\eta\Phi_1 + \xi_s(\theta)\xi_s'(\theta)\partial_\eta\partial_s\Phi_1 + \partial_s[\xi_s(\theta)\xi_s'(\theta)\partial_\eta\Phi_1] \\
&\quad + \lambda[g''(\Phi_0)\Phi_1 U_0 + g'(\Phi_0)U_1] + \partial_s\{[\xi_s(\theta)^2 + \xi_s'(\theta)^2 + \xi_s(\theta)\xi_s''(\theta)]\partial_s\Phi_0\} \\
&\quad - \eta\,\mathcal{K}\{\partial_\eta[\xi_s(\theta)\xi_s'(\theta)\partial_s\Phi_0] + \partial_s[\xi_s(\theta)\xi_s'(\theta)\partial_\eta\Phi_0]\} - \eta\mathcal{K}^2\xi_s(\theta)^2\partial_\eta\Phi_0. \qquad \text{(A41)}
\end{aligned}
$$

Note that the previous equation has again the form $\mathcal{L}\Phi_2 = \mathcal{G}_2$. As before, the right-hand side has to be orthogonal to $\partial_\eta\Phi_0$. Despite its very complex form, this condition can be greatly simplified by noticing that the odd terms will not contribute to the orthogonality condition. Note also that since $\mathcal{L}$ is an even operator and it is easy to prove that the right hand side of Eq. (A36) is also even, Φ_1 will be even too.

Taking this into consideration, the orthogonality condition takes the following very simple form:

$$-\alpha v_n \tau_1(\theta) \int_{-\infty}^{\infty} d\eta (\partial_\eta \Phi_0)^2 = \lambda \int_{-\infty}^{\infty} d\eta\, \partial_\eta \Phi_0\, g'(\Phi_0) U_1. \tag{A42}$$

From the diffusion equation, which will be needed to find the second-order correction to the flux across the interface, we have the following:

$$-v_n \partial_\eta U_1 + \partial_t U_0 - v_t \partial_s U_0 = D_{nn} \partial_\eta^2 U_2 + D_{tt} \mathcal{K} \partial_\eta U_1 + 2 D_{nt} \partial_\eta \partial_s U_1 + D_{tt} \partial_s^2 U_0 - 2 D_{nt} \mathcal{K} \partial_s U_0 + f - \frac{U_0}{\tau_v} + v_n \partial_\eta \Phi_1 + v_t \partial_s \Phi_0. \tag{A43}$$

In order to obtain a useful correction from the previous equation, we will have to make use of the matching conditions between the inner and the outer problem.

d. Matching conditions

$$\lim_{\eta \to \pm\infty} [U_0(\eta,s)] - \tilde{u}_0|^{\pm} = 0, \tag{A44a}$$

$$\lim_{\eta \to \pm\infty} [U_1(\eta,s) - (\tilde{u}_1|^{\pm} + \eta \partial_r \tilde{u}_0|^{\pm})] = 0, \tag{A44b}$$

$$\lim_{\eta \to \pm\infty} \left[U_2(\eta,s) - \left(\tilde{u}_2|^{\pm} + \eta \partial_r \tilde{u}_1|^{\pm} + \frac{\eta^2}{2} \partial_r^2 \tilde{u}_0|^{\pm} \right) \right] = 0. \tag{A44c}$$

Also, immediately one can obtain that

$$\partial_r \tilde{u}_0|^{\pm} = \lim_{\eta \to \pm\infty} \partial_\eta U_1(\eta,s), \tag{A45a}$$

$$\partial_s \tilde{u}_0|^{\pm} = \lim_{\eta \to \pm\infty} \partial_s U_0(\eta,s), \tag{A45b}$$

$$\partial_r \tilde{u}_1|^{\pm} = \lim_{\eta \to \pm\infty} \left[\partial_\eta U_2(\eta,s) - \eta \partial_r^2 \tilde{u}_0|^{\pm} \right], \tag{A45c}$$

$$\partial_s \tilde{u}_1|^{\pm} = \lim_{\eta \to \pm\infty} [\partial_s U_1(\eta,s) - \eta \partial_r \partial_s \tilde{u}_0|^{\pm}]. \tag{A45d}$$

While we do not write the arguments of the outer functions in the interface, it is understood that they depend on s.

e. Adatom conservation

In this section we prove that the jump discontinuity for the adatom flux is what could be expected from a conservation equation, at least to second order. We start by computing the flux to zero order in the outer expansion.

According to the matching condition (A45a), by using Eq. (A40) we have that

$$\partial_r \tilde{u}_0|^{+} = \lim_{\eta \to +\infty} \partial_\eta U_1(\eta,s) = \frac{A}{D_{nn}}, \tag{A46a}$$

$$\partial_r \tilde{u}_0|^{-} = \lim_{\eta \to -\infty} \partial_\eta U_1(\eta,s) = \frac{1}{D_{nn}}(A - v_n). \tag{A46b}$$

From (A45b) we have that

$$\partial_s \tilde{u}_0|^{+} = \partial_s \tilde{u}_0|^{-} = \partial_s \bar{U}_0(s), \tag{A47}$$

which does not change across the interface.

From Appendix A1 the jump condition follows as $r \to 0^{\pm}$:

$$[\mathbf{n} \cdot \mathrm{D} \nabla \tilde{u}_0]^{\pm} = [D_{nn} \partial_r \tilde{u}_0 + D_{nt} \partial_s \tilde{u}_0]^{\pm} = v_n, \tag{A48}$$

which is what we expected. Nevertheless, we have performed a higher-order expansion, and we have to make sure that the additional terms added will not change the previous equation.

Second-order correction. Now it is proved that going to a higher order does not change Eq. (A48), and that the correction is bounded.

To do so the two derivatives of $\tilde{u}_1$ with respect to r and s have to be computed. We start with the derivative with respect to s, as it can be computed from what we have done already. From the matching condition (A45d) we have that

$$\begin{aligned}
\partial_s \tilde{u}_1|^{+} &= \lim_{\eta \to +\infty} (\partial_s U_1(\eta,s) - \eta \partial_r \partial_s \tilde{u}_0|^{+}) \\
&= \lim_{\eta \to +\infty} \left[\partial_s \bar{U}_1 + \partial_s \left(\frac{A}{D_{nn}} \right) \eta \right. \\
&\quad - \partial_s \left(\frac{v_n}{D_{nn}} \right) \int_0^{\eta} d\bar{\eta} \Phi_0(\bar{\eta}) - \frac{v_n}{D_{nn}} \int_0^{\eta} d\bar{\eta} \partial_s \Phi_0(\bar{\eta}) \\
&\quad \left. - \eta\, \partial_s \left(\frac{A}{D_{nn}} \right) \right] \\
&= \partial_s \bar{U}_1 - \partial_s \left(\frac{v_n}{D_{nn}} \right) \int_0^{\infty} d\bar{\eta} \Phi_0(\bar{\eta}) \\
&\quad + \mathcal{K} \frac{v_n}{D_{nn}} \frac{\xi'}{\xi} \int_0^{\infty} d\bar{\eta} \bar{\eta} \partial_\eta \Phi_0(\bar{\eta}).
\end{aligned} \tag{A49}$$

Similarly, one can show that

$$\begin{aligned}
\partial_s \tilde{u}_1|^{-} &= \partial_s \bar{U}_1 - \partial_s \left(\frac{v_n}{D_{nn}} \right) \int_0^{-\infty} d\bar{\eta} [\Phi_0(\bar{\eta}) - 1] \\
&\quad + \mathcal{K} \frac{v_n}{D_{nn}} \frac{\xi'}{\xi} \int_0^{-\infty} d\bar{\eta} \bar{\eta} \partial_\eta \Phi_0(\bar{\eta}).
\end{aligned} \tag{A50}$$

The relevant integrals are discussed in the next section. For now, it is enough to notice that

$$\begin{aligned}
\int_0^{\infty} d\bar{\eta} \Phi_0(\bar{\eta}) &= \int_0^{\infty} d\bar{\eta} [1 - \Phi_0(-\bar{\eta})] \\
&= \int_0^{-\infty} d\bar{\eta} [\Phi_0(\bar{\eta}) - 1].
\end{aligned} \tag{A51}$$

The first equality stems from the symmetry $\Phi_0(\eta) = 1 - \Phi_0(-\eta)$ and the second from changing the sign of the integration variable. Similarly,

$$\int_0^{\infty} d\bar{\eta} \bar{\eta} \partial_\eta \Phi_0(\bar{\eta}) = \int_0^{-\infty} d\bar{\eta} \bar{\eta} \partial_\eta \Phi_0(\bar{\eta}), \tag{A52}$$

which again follows from a change of sign in the integration variable and the fact that $\partial_\eta \Phi_0$ is even. The previous relations

prove that $\partial_s \tilde{u}_1|^+ = \partial_s \tilde{u}_1|^-$ and hence that this derivative will not contribute to the jump discontinuity.

Now, in order to find $\partial_r \tilde{u}_1|^\pm$ Eq. (A45c) implies that we need to know $\partial_\eta U_2$. For that reason we bring in Eq. (A43), which, after an integration with respect to η, takes the following form:

$$\eta\left(-f + \frac{U_0}{\tau_v} - D_{tt}\partial_s^2 U_0 + 2D_{nt}\mathcal{K}\partial_s U_0 + \partial_t U_0 - v_t \partial_s U_0\right) = A_2(s) + D_{nn}\partial_\eta U_2 + (D_{tt}\mathcal{K} + v_n)U_1 + 2D_{nt}\partial_s U_1 + v_n \Phi_1 + v_t \int_0^\eta d\bar{\eta}\partial_s \Phi_0, \tag{A53}$$

where all the integration constants have been amalgamated in $A_2(s)$.

Clearly, the LHS of the previous equation has the same structure as Eq. (A26). If we multiply the latter by η and subtract it from the former the following result is obtained automatically, after taking the limit $\eta \to \pm\infty$:

$$-A_2(s) = \partial_r \tilde{u}_1|^\pm + (D_{tt}\mathcal{K} + v_n)\tilde{u}_1|^\pm + 2D_{nt}\partial_s \tilde{u}_1|^\pm + v_t \int_0^{\pm\infty} d\bar{\eta}\,\partial_s \Phi_0, \tag{A54}$$

where we have made use of the fact that each term in the LHS of (A26) matches its counterpart in (A53) by matching condition (A44a). We have also used the matching conditions (A44b), (A45c), and (A45d). Finally, Φ_1 goes to zero as $\eta \to \pm\infty$, which can also be deduced from the matching with the outer solution.

Most of the terms present in Eq. (A54) have been discussed already, including the $\partial_s \tilde{u}_1|^\pm$ term and the integral, and it has been proved that they do not change across the interface. The only term that it is left to check is $\tilde{u}_1|^\pm$:

$$\tilde{u}_1|^+ = \lim_{\eta\to+\infty}(U_1(\eta,s) - \eta\partial_r \tilde{u}_0|^+) = \bar{U}_1 - \frac{v_n}{D_{nn}}\int_0^\infty d\bar{\eta}\,\Phi_0(\bar{\eta}), \tag{A55a}$$

$$\tilde{u}_1|^- = \lim_{\eta\to-\infty}(U_1(\eta,s) - \eta\partial_r \tilde{u}_0|^-) = \bar{U}_1 - \frac{v_n}{D_{nn}}\int_0^{-\infty} d\bar{\eta}(\Phi_0(\bar{\eta}) - 1), \tag{A55b}$$

and it has already been proven in Eq. (A51) that the integrals in both limits are identical.

This concludes the proof that $\partial_r \tilde{u}_1|^+ = \partial_r \tilde{u}_1|^-$. The derivative can be computed on either side, and takes the following form:

$$\partial_r \tilde{u}_1|^\pm = -\mathcal{K}\left(2D_{nt}\frac{v_n}{D_{nn}} - v_t\right)\frac{\partial_\theta \xi}{\xi}\int_0^\infty d\bar{\eta}\,\bar{\eta}\,\partial_\eta \Phi_0(\bar{\eta}) - (D_{tt}\mathcal{K} + v_n)\left(\bar{U}_1 - \frac{v_n}{D_{nn}}\int_0^\infty d\bar{\eta}\,\Phi_0(\bar{\eta})\right) - 2D_{nt}\partial_s \bar{U}_1 + 2D_{nt}\partial_s\left(\frac{v_n}{D_{nn}}\right)\int_0^\infty d\bar{\eta}\,\Phi_0(\bar{\eta}) - A_2(s). \tag{A56}$$

Finally, we can write the conservation condition as follows:

$$[\mathbf{n}\cdot \mathrm{D}\nabla(\tilde{u}_0 + \epsilon\tilde{u}_1)]^\pm = v_n, \tag{A57}$$

so that the conservation condition is correct to order $O(\epsilon^2)$.

f. Gibbs-Thomson

Now we prove that the Gibbs-Thomson equation is correctly reproduced in the sharp interface limit. From Eq. (A37) by using (A32) we obtain the following:

$$\left\{\alpha v_n \frac{\tau_0(\theta)}{\xi_s(\theta)} + \left[\xi_s(\theta) + \xi_s''(\theta)\right]\mathcal{K}\right\}\int_0^1 d\phi\sqrt{2f(\phi)} - \lambda U_0 \int_0^1 d\phi\, g'(\phi) = 0, \tag{A58}$$

or

$$\tilde{u}_0|^\pm = \lim_{\eta\to\pm\infty} U_0 = \frac{\alpha}{\lambda}v_n\frac{\tau_0(\theta)}{\xi_s(\theta)}\frac{I}{J} + \frac{1}{\lambda}\frac{I}{J}(\xi_s(\theta) + \xi_s''(\theta))\mathcal{K}, \tag{A59}$$

where we have defined

$$I = \xi_s(\theta)\int_{-\infty}^\infty d\eta(\partial_\eta \Phi_0)^2 = \int_0^1 d\phi\sqrt{2f(\phi)}, \tag{A60}$$

$$J = -\int_{-\infty}^\infty d\eta\,\partial_\eta \Phi_0\, g'(\Phi_0) = \int_0^1 d\phi\, g'(\phi). \tag{A61}$$

Second-order correction. As in the preceding section, we can improve the previous result with a second-order correction, which in this case will be nonzero. From (A42) and (A40) we have the following:

$$-\alpha v_n \frac{\tau_1(\theta)}{\xi_s(\theta)}\int_0^1 d\phi\sqrt{2f(\phi)} = -\lambda\bar{U}_1\int_0^1 d\phi\, g'(\phi) - \frac{\lambda\xi_s(\theta)v_n}{D_{nn}}\int_0^1 d\phi\, g'(\phi)\int_{\frac{1}{2}}^\phi d\bar{\phi}\frac{\bar{\phi}}{\sqrt{2f(\bar{\phi})}}, \tag{A62}$$

where we have used (A32) and the fact that $\partial_\eta \Phi_0\, g'(\Phi_0)$ is even in the integration interval. Equation (A62) implies that

$$\bar{U}_1 = \frac{\alpha v_n}{\lambda}\frac{\tau_1(\theta)}{\xi_s(\theta)}\frac{I}{J} - \frac{\xi_s(\theta)v_n}{D_{nn}}\frac{K}{J}, \tag{A63}$$

with the substitution

$$K = \frac{1}{\xi_s(\theta)}\int_{-\infty}^\infty d\eta\,\partial_\eta \Phi_0\, g'(\Phi_0)\int_0^\eta d\bar{\eta}\,\Phi_0(\bar{\eta}) = \int_0^1 d\phi\, g'(\phi)\int_{\frac{1}{2}}^\phi d\bar{\phi}\frac{\bar{\phi}}{\sqrt{2f(\bar{\phi})}}. \tag{A64}$$

Now, according to (A55b) we have that

$$\tilde{u}_1|^\pm = \bar{U}_1 + \frac{\xi_s(\theta)v_n}{D_{nn}}\int_{\frac{1}{2}}^0 d\bar{\phi}\frac{\bar{\phi}}{\sqrt{2f(\bar{\phi})}} = \frac{\alpha v_n}{\lambda}\frac{\tau_1(\theta)}{\xi_s(\theta)}\frac{I}{J} - \frac{\xi_s(\theta)v_n}{D_{nn}}\left(\frac{K}{J} + F\right), \tag{A65}$$

where F is defined as

$$F = \frac{1}{\xi_s(\theta)}\int_0^{-\infty} d\bar{\eta}[\Phi_0(\bar{\eta}) - 1] = \int_0^{\frac{1}{2}} d\bar{\phi}\frac{\bar{\phi}}{\sqrt{2f(\bar{\phi})}}. \tag{A66}$$

Finally, we are left with the Gibbs-Thomson condition:

$$\tilde{u}|^\pm \approx \tilde{u}_0|^\pm + \epsilon\tilde{u}_1|^\pm = \frac{1}{\lambda}\frac{I}{J}[\xi_s(\theta) + \xi_s''(\theta)]\mathcal{K} + \frac{v_n\alpha}{\xi_s(\theta)\lambda}[\tau_0(\theta) + \epsilon\tau_1(\theta)]\frac{I}{J} - \epsilon\frac{\xi_s(\theta)v_n}{D_{nn}}\left(\frac{K}{J} + F\right). \tag{A67}$$

g. Summary

If we define the two numerical constants $a_1 = I/J$ and $a_2 = K/J + F$ we can rewrite Eqs. (A67) and (A57) as follows:

$$\tilde{u}|^{\pm} \approx \frac{v_n \alpha}{\xi_s(\theta)\lambda}[\tau_0(\theta) + \epsilon\tau_1(\theta)]a_1 - \epsilon\frac{\xi_s(\theta)v_n}{D_{nn}}a_2 + \frac{1}{\lambda}a_1[\xi_s(\theta) + \xi_s''(\theta)]\mathcal{K} \tag{A68}$$

$$v_n = [\mathbf{n}\cdot \mathrm{D}\nabla(\tilde{u})]^{\pm}. \tag{A69}$$

Clearly, the previous equations have the same form as the sharp interface boundary conditions (13) and (12). This allows us to make the following identifications:

$$\lambda = \frac{a_1}{d_0}, \tag{A70}$$

$$\alpha = \frac{\beta}{d_0}, \tag{A71}$$

$$\tau_0(\theta) = \xi_s(\theta)\xi_k(\theta), \tag{A72}$$

where $\xi_k(\theta)$ is the kinetic anisotropy.

In order to cancel the first order in ϵ correction and to make the problem correct to second order, we have to make the following identification:

$$\tau_1(\theta) = \frac{\xi_s(\theta)^2}{\beta D_{nn}(\theta)}a_2, \tag{A73}$$

which requires the explicit computation of $D_{nn}(\theta)$, by using the formulas of Appendix A1b.

Finally, note that the previous formulas make use of the sharp-interface angle θ, as opposed to Θ, which is the angle that can be computed from the phase field. A careful analysis of the differences between these two descriptions shows that these differences do not contribute the the formulas obtained above.

APPENDIX B: NUMERICAL MESH

In this Appendix we illustrate the process of adaptation of the grid. In all cases, there is a base grid of size 64×64, covering the domain $[-8,8] \times [-8,8]$ in the units of the problem.

Successive refinements of the computational grid that divide mesh spacing by a factor of two, are computed where they are needed, where the gradient of u or the gradient of ϕ has a value higher than a given threshold. The grid adaptation algorithm of Ref. [43] is used.

The small value of the ϵ parameter in this problem needed for the phase-field model to accurately approximate the sharp interface problem requires several levels of refinement. We have used in all simulations seven levels of refinement, resulting in the ratio $\Delta x_{\min}/\Delta x_{\max} = 2^{-7}$, as we show in Fig. 8.

In Fig. 8, we show the dynamic adaptive mesh for Fig. 6(b), the sixfold case with $\delta = 0$. In the first panel we show the root grid and the next two levels of refinement and then in the subsequent panels we zoom in several times, by adding the representation of a higher level grid each time, in such a way that the highest-order grid has the same lattice spacing in all cases. We see that the different refinements of the grid concentrate on the interface, as expected.

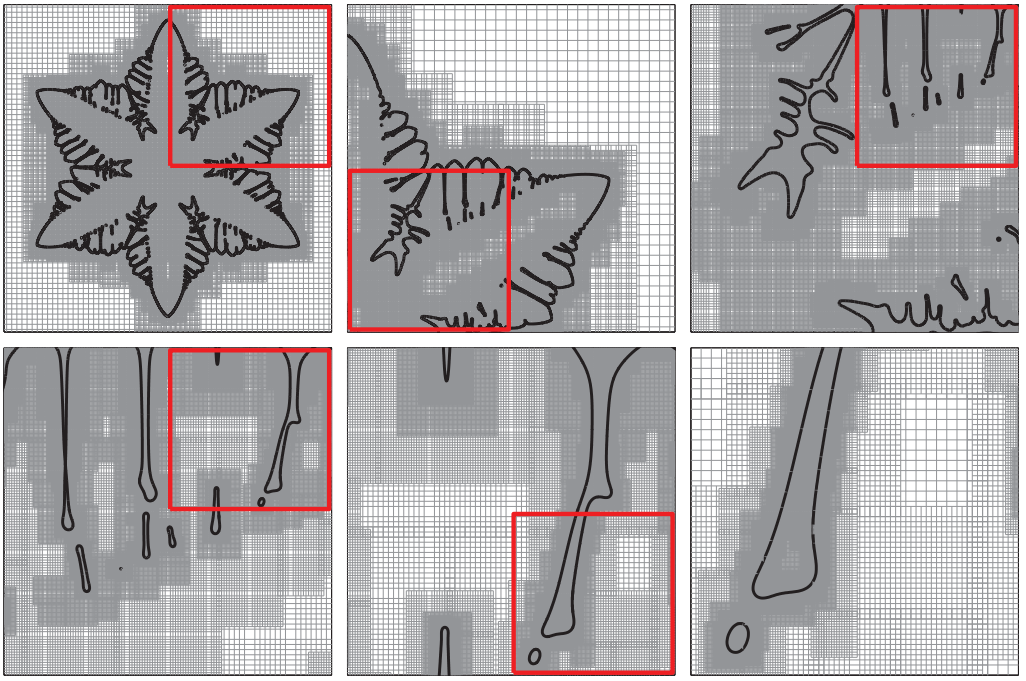

FIG. 8. (Color online) Example of grid adaptation for the case $\delta = 0$ from Fig. 6(b). From left to right, and from top to bottom we show different levels of magnification. Each subfigure has a magnification of $2\times$ with respect to the previous one, and the area magnified is represented as a thick red square. For each subfigure we add another subgrid, in such a way that the lattice spacing of the finer grid is always the same.

[1] T. Michely and J. Krug, *Islands, Mounds, and Atoms: Patterns and Processes in Crystal Growth Far from Equilibrium*, Springer Series in Surface Sciences Series (Springer-Verlag, Berlin, 2004).

[2] J. W. Evans, P. A. Thiel, and M. C. Bartelt, Surf. Sci. Rep. **61**, 1 (2006).

[3] C. Mattevi, H. Kim, and M. Chhowalla, J. Materials Chem. **21**, 3324 (2011).

[4] B. Wu, D. Geng, Z. Xu, Y. Guo, L. Huang, Y. Xue, J. Chen, G. Yu, and Y. Liu, Npg Asia Materials **5**, e36 (2013).

[5] Q. Li, H. Chou, J.-H. Zhong, J.-Y. Liu, A. Dolocan, J. Zhang, Y. Zhou, R. S. Ruoff, S. Chen, and W. Cai, Nano Lett. **13**, 486 (2013).

[6] I. Shvets, S. Murphy, and V. Kalinin, Surf. Sci. **601**, 3169 (2007).

[7] Y. Han, D. Jing, B. Ünal, P. A. Thiel, and J. W. Evans, Phys. Rev. B **84**, 113414 (2011).

[8] Y. Han, S. M. Russell, A. R. Layson, H. Walen, C. D. Yuen, P. A. Thiel, and J. W. Evans, Phys. Rev. B **87**, 155420 (2013).

[9] F. C. Frank, in *Growth and Perfection of Crystals*, edited by R. H. Doremus (Wiley, New York, 1958), p. 411.

[10] E. Yokoyama and R. F. Sekerka, J. Cryst. Growth **125**, 389 (1992).

[11] R. F. Sekerka, J. Cryst. Growth **264**, 530 (2004).

[12] W. K. Burton, N. Cabrera, and F. C. Frank, Philos. Trans. R. Soc. London A **243**, 299 (1951).

[13] A. Karma and M. Plapp, Phys. Rev. Lett. **81**, 4444 (1998).

[14] O. Pierre-Louis, Phys. Rev. E **68**, 021604 (2003).

[15] Z. Hu, J. S. Lowengrub, S. M. Wise, and A. Voigt, Phys. Nonlinear Phenom. **241**, 77 (2012).

[16] A. Karma and W. J. Rappel, Phys. Rev. E **57**, 4323 (1998).

[17] J. Bragard, A. Karma, Y. H. Lee, and M. Plapp, Interface Sci. **10**, 121 (2002).

[18] A. M. Mullis, Acta Mater. **51**, 1959 (2003).

[19] R. Gomer, Rep. Prog. Phys. **53**, 917 (1990).

[20] T. Ala-Nissila and S. C. Ying, Prog. Surf. Sci. **39**, 227 (1992).

[21] X. D. Xiao, X. D. Zhu, W. Daum, and Y. R. Shen, Phys. Rev. Lett. **66**, 2352 (1991).

[22] M. Sato, M. Uwaha, Y. Saito, and Y. Hirose, Phys. Rev. B **67**, 125408 (2003).

[23] G. Danker, O. Pierre-Louis, K. Kassner, and C. Misbah, Phys. Rev. E **68**, 020601 (2003).

[24] G. Danker, O. Pierre-Louis, K. Kassner, and C. Misbah, Phys. Rev. Lett. **93**, 185504 (2004).

[25] T. Frisch and A. Verga, Phys. Rev. Lett. **96**, 166104 (2006).

[26] M. Guedda, H. Trojette, S. Peponas, and M. Benlahsen, Phys. Rev. B **81**, 195436 (2010).

[27] G. S. Bales and A. Zangwill, Phys. Rev. B **41**, 5500 (1990).

[28] C. Misbah, O. Pierre-Louis, and Y. Saito, Rev. Mod. Phys. **82**, 981 (2010).

[29] T. Ala-Nissila, R. Ferrando, and S. C. Ying, Adv. Phys. **51**, 949 (2002).

[30] G. B. McFadden, A. A. Wheeler, R. J. Braun, S. R. Coriell, and R. F. Sekerka, Phys. Rev. E **48**, 2016 (1993).

[31] R. Gonzalez-Cinca, L. Ramirez-Piscina, J. Casademunt, A. Hernandez-Machado, T. Toth-Katona, T. Borzsonyi, and A. Buka, J. Crystal Growth **193**, 712 (1998).

[32] A. Shibkov, M. Zheltov, A. Korolev, A. Kazakov, and A. Leonov, J. Cryst. Growth **285**, 215 (2005).

[33] J. Krug, in *Multiscale Modeling in Epitaxial Growth*, ISNM International Series of Numerical Mathematics Vol. 149, edited by A. Voigt (Birkhäuser, Basel, 2005), pp. 69–95.

[34] A. Pimpinelli and J. Villain, *Physics of Crystal Growth*, Collection Alea-Saclay: Monographs and Texts in Statistical Physics (Cambridge University Press, Cambridge, 1998).

[35] S. Wise, J. Kim, and J. Lowengrub, J. Comput. Phys. **226**, 414 (2007).

[36] T. Ihle, European Phys. J. B **16**, 337 (2000).

[37] S. Dieluweit, H. Ibach, M. Giesen, and T. L. Einstein, Phys. Rev. B **67**, 121410 (2003).

[38] A. B. Pang, K. L. Man, M. S. Altman, T. J. Stasevich, F. Szalma, and T. L. Einstein, Phys. Rev. B **77**, 115424 (2008).

[39] J. H. Neave, P. J. Dobson, B. A. Joyce, and J. Zhang, Appl. Phys. Lett. **47**, 100 (1985).

[40] Y. W. Mo, J. Kleiner, M. B. Webb, and M. G. Lagally, Phys. Rev. Lett. **66**, 1998 (1991).

[41] K. N. Tu, J. Appl. Phys. **94**, 5451 (2003).

[42] W. W. Mullins and R. F. Sekerka, J. Appl. Phys. **34**, 323 (1963).

[43] M. Berger and I. Rigoutsos, IEEE Transactions On Systems Man Cybernetics **21**, 1278 (1991).

[44] K. Vetsigian and N. Goldenfeld, Phys. Rev. E **68**, 060601 (2003).

[45] M. Plapp, Philos. Mag. **91**, 25 (2011).

[46] M. Nicoli, M. Plapp, and H. Henry, Phys. Rev. E **84**, 046707 (2011).

[47] M. Ozdemir and A. Zangwill, Phys. Rev. B **45**, 3718 (1992).

[48] S. Tanaka, N. C. Bartelt, C. C. Umbach, R. M. Tromp, and J. M. Blakely, Phys. Rev. Lett. **78**, 3342 (1997).

[49] J. J. Metois and S. Stoyanov, Surf. Science **440**, 407 (1999).

[50] S. Stoyanov and V. Tonchev, Phys. Rev. B **58**, 1590 (1998).

[51] D. M. Ackerman and J. W. Evans, Multiscale Modeling and Simulation **9**, 59 (2011).